The CHAOS-4 Geomagnetic Field Model
Draft, May 7, 2012

Nils Olsen[1], Hermann Lühr[2], Terence J. Sabaka[3], Ingo Michaelis[2], Jan Rauberg[2], Lars Tøffner-Clausen[1], Chris C. Finlay[1]

Abstract. We present CHAOS-4, a new version in the CHAOS model series, which aims to describe the Earth's magnetic field with high spatial resolution (terms up to spherical degree $n = 85$ for the crustal field, and up to $n = 16$ for the time-varying core field are robustly determined).

More than 11 years of data from the satellite Ørsted, CHAMP and SAC-C satellites, augmented with ground observatory monthly mean values have been used for this model. Maximum spherical harmonic degree of the static (crustal) field is $n = 100$. The core field time changes are expressed by spherical harmonic expansion coefficients up to $n = 20$, described by order 6 splines (with 6-month knot spacing) spanning the time interval 1997.0 to 2012.5. The third time derivative of the squared magnetic field intensity is regularized at the core-mantle boundary. No spatial regularization is applied for the core field, but the high-degree crustal field is regularized for $n > 85$.

The final CHAOS-4 model is derived by merging two sub-models: its low-degree part has been derived using similar model parametrization and data sets as used for previous CHAOS models (but of course including newer satellite observations), while its high-degree crustal field part is solely determined from low-altitude CHAMP satellite observations after 2009. The god agreement with the MF7 model for degrees up to degree $n = 80$ confirms that crustal field structures down to a horizontal wavelength of 500 km are currently robustly determined.

1. Introduction

More than 10 years of continuous magnetic field measurements obtained by the Ørsted and CHAMP satellites enable outstanding opportunities to investigate the Earth's magnetic field, both regarding rapid changes of the core field (secular variation) and the determination of the magnetic field due to lithospheric magnetization.

Of special interest for deriving the small-scale structure of the lithospheric field are the measurements obtained during the last months of the CHAMP satellite mission, when satellite altitude was below 300 km.

In the present paper we describe CHAOS-4, a model of the geomagnetic field obtained from CHAMP data obtained between the launch of the satellite in July 2000 until its atmospheric re-entry in September 2010. In addition, we also use Ørsted and SAC-C satellite measurements and ground observatory data for this model.

The benefit of low-altitude CHAMP observations for determining the lithospheric field is obvious from Figure 1 which shows the spatial powerspectrum of the geomagnetic field at various altitudes. The black curve is the spectrum at Earth's surface (according to the CHAOS-4 model presented in this article), while the colored curves present spectra at various altitudes of the CHAMP satellite (blue curves) and of the Ørsted satellite (red curve).

[1]DTU Space, Technical University of Denmark, Juliane Maries Vej 30, 2100 Copenhagen, Denmark.

[2]Helmholtz-Zentrum Potsdam, Deutsches GeoForschungsZentrum, 14473 Potsdam, Germany.

[3]Geodynamics Branch, NASA GSFC, Greenbelt/MD, USA.

Let us assume that measuring conditions (which includes instrument errors, external field disturbances, and spatio-temporal sampling) are such that magnetic field structures of squared amplitudes larger than 0.1 nT^2 can be resolved. Under this assumption only features up to spherical harmonic degree $n = 20$ can be determined from data obtained by a satellite (like Ørsted) at an altitude of 750 km. In contrast, data from CHAMP at the beginning of the mission, when altitude was about 450 km altitude, would allow for a determination of the the lithospheric field up to $n = 40$. Data taken at 300 km altitude (which was CHAMP mean altitude at the beginning of 2010) would allow for determining models up to $n = 60$. Finally, taking advantage of the very-low altitude data of the last weeks of CHAMP mission lifetime, as done in this paper, would allow the lithospheric field to be resolved up to $n = 80$. Note that the threshold value of 0.1 nT^2 that we have chosen here is for illustration purposes only; we do not claim that this is the actual limit of the satellite observations.

As described in the review article by *Thébault et al.* [2010], two complementary philosophies are in use for deriving spherical harmonic models of the Earth's crustal field: In the sequential approach, *a-priori* models of all known magnetic field contributions but the crustal field are subtracted from the data, followed by a careful data selection and applying empirical corrections. The different versions in the MF model series of Stefan Maus and co-workers are examples of models derived using this approach. They are derived from CHAMP observations which have been along-track filtered after removal of *a-priori* models of the core field and of the ocean tidal magnetic signal. MF6, the most recent published model version [*Maus et al.*, 2008], also includes line leveling between adjacent satellite tracks, which minimizes the variance between close encounters. This model formally describes the crustal field up to spherical harmonic degree $n = 120$ (corresponding to 333 km horizontal wavelength),
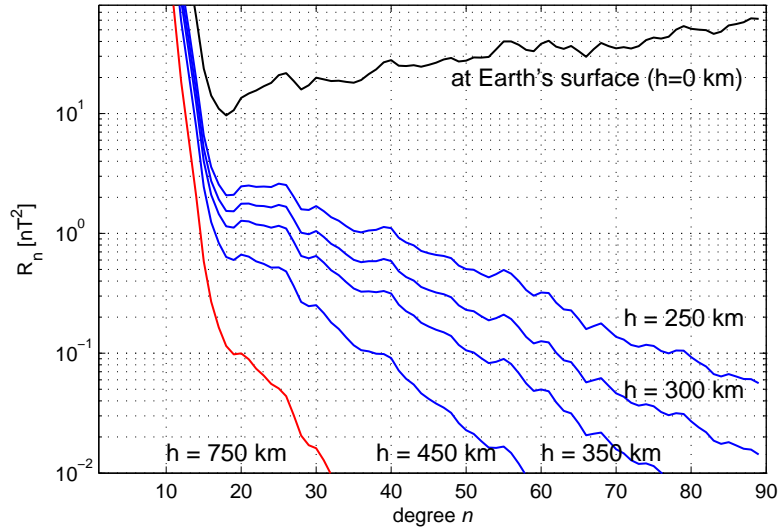
Figure 1. Spatial power spectrum of the geomagnetic field at Earth's surface (black curve) and at various altitudes of CHAMP (blue). Also shown is the spectrum at a mean altitude of the Ørsted satellite of 750 km (red).

but coefficients above $n > 80$ are damped (regularized) and thus probably not robustly resolved. A new (unpublished) version, MF7 [*Maus*, 2010], describes the field formally up to $n = 133$.

Contrary to this serial approach, the comprehensive approach aims at solving simultaneously for all major internal and external field contributions. Examples of models derived using this approach are the CM models [e.g., *Sabaka et al.*, 2004], and, using more recent satellite data, the GRIMM models [*Lesur et al.*, 2008; *Lesur et al.*, 2010], the BGS models [*Thomson and Lesur*, 2007; *Thomson et al.*, 2010], and the CHAOS models [*Olsen et al.*, 2006, 2009, 2010].

Until recently, the altitude of the CHAMP satellite was not sufficiently low to determine small-scale structures of the crustal field without along-track filtering of the data (to remove unmodeled external field contributions), and hence only terms up to spherical harmonic degree $n = 50$ or so could be determined robustly using the comprehensive approach. Inclusion of the most recent low-altitude CHAMP data, as done here, allows us to determine the crustal field up to spherical harmonic degree $n = 90$ or so.

The CHAOS-4 field model presented here is the most recent version in the CHAOS model series. Previous versions are CHAOS [*Olsen et al.*, 2006], xCHAOS [*Olsen and Mandea*, 2008], CHAOS-2 [*Olsen et al.*, 2009] and CHAOS-3 [*Olsen et al.*, 2010]. For the previous model versions we have concentrated on an optimal description of the core field and its temporal resolution; the static (crustal) field was only modeled up to relatively low spherical harmonic degrees ($n = 60$ at most). For CHAOS-4 we extend the spherical harmonic degrees and solve for the crustal field up to $n = 100$.

CHAOS-4 is derived by merging two models, which both are determined using the comprehensive approach but from different data sets (and using different model parameterization): spherical harmonic coefficients of the CHAOS-4 model up to degree $n = 24$ (which includes the time-changes of the core field) are taken from model version CHAOS-4l, while coefficients describing the crustal field for $n = 25 - 100$ are taken from model version CHAOS-4h. The former is derived in the tradition of the other versions of the CHAOS series by using data from all three satellites Ørsted, CHAMP and SAC-C together with observatory monthly mean values, while CHAOS-4h is derived solely from the most recent low altitude CHAMP satellite data.

2. Data and model parameterization

We use Ørsted scalar data between March 1999 and July 2010, and vector data between March 1999 and December 2004; CHAMP scalar data between August 2000 and August 2010, and vector data between January 2001 and August 2010; and SAC-C scalar data between January 2001 and December 2004. Similar data selection criteria to those chosen for determining the previous versions in the CHAOS model series have been used; the main modification concerns the inclusion of pre-midnight CHAMP data (for previous CHAOS versions we only used post-midnight non-polar CHAMP data to avoid contamination of the crustal field determination by plasma irregularities. However, they are almost absent during the solar minimum conditions of the recent years, allowing us to include also pre-midnight data).

In particular: 1) we use only data from dark regions (sun $10°$ below horizon) and for which the D_{st}-index measuring the strength of the magnetospheric ring-current does not change by more than 2 nT/hr; 2) at non-polar latitudes (equatorward of $\pm 60°$ dipole latitude) we require for the geomagnetic activity index $Kp \leq 2^o$, while for regions poleward of $60°$ dipole latitude the merging electric field at the magnetopause has to be less than 0.8 mV/m; 2) vector data are taken for dipole latitudes equatorward of $\pm 60^o$, while data are used for regions poleward of $\pm 60°$ or if attitude data were not available; 3) non-polar CHAMP data are only used for periods when the electron density is $N_e < 10^{-5}$ cm^{-3}, to minimize the influence of plasma bubbles [*Stolle et al.*, 2006]. This condition is fulfilled for almost all times during the recent solar minimum years 2006 to 2010.

Data weights proportional to $\sin \theta$ (where θ is geographic co-latitude) are applied to simulate an equal-area distribution. Anisotropic errors due to attitude uncertainty [*Holme and Bloxham*, 1996; *Holme*, 2000] are considered for all Ørsted vector data and for CHAMP vector data when attitude data from only one star imager are available.

To extend the model back in time beyond February 1999 we supplement the satellite data with annual differences of revised observatory monthly means of the North, East and Vertical downward components (X, Y, Z) for the time interval 1997.0 - 2009.5. these data are the same as those used for CHAOS-3; see *Olsen et al.* [2010] for details.

As described above, the very recent low-altitude CHAMP observations are crucial for a robust determination of small-scale crustal field structures. But how has CHAMP altitude
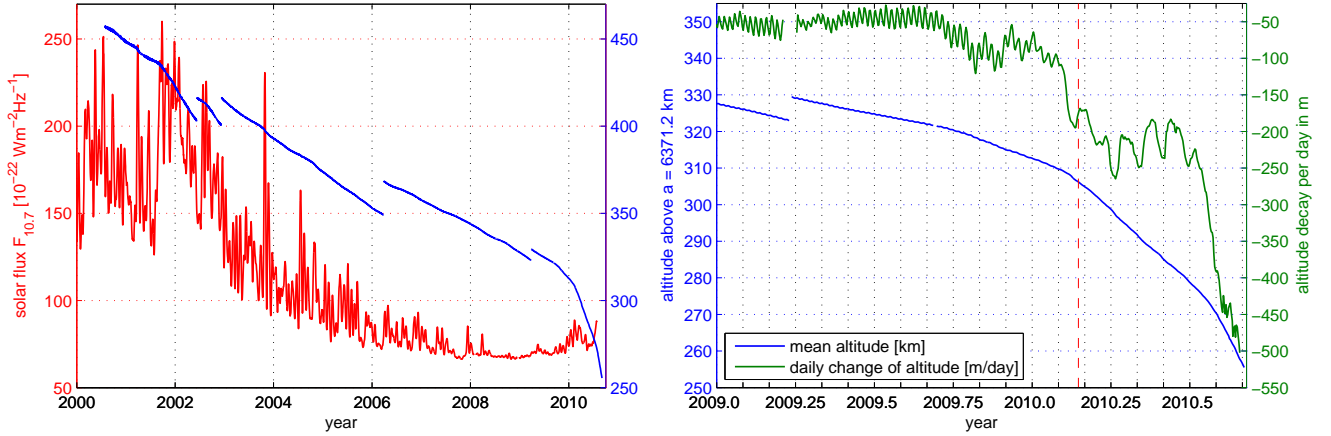
Figure 2. Left: $F_{10.7}$ solar flux (red) and CHAMP mean altitude (blue) in dependence on time. Right: CHAMP mean altitude (blue) and mean daily altitude decay (green) since 2009.

evolved with time? The left part of Figure 2 shows in blue the mean altitude of CHAMP (with respect to a mean Earth radius of $a = 6371.2$ km), together with the temporal evolution of the $F_{10.7}$ solar flux (red curve). Various altitude maneuvers are the reason for the sudden increase of altitude of the satellite. Note how the increased solar activity at the end of 2001 leads to a faster altitude decay, due to increased air density and thereby increased air-drag.

The altitude of the satellite was about 350 km during the solar minimum years 2007 to 2009, and reached 300 km at the beginning of 2010. Satellite altitude for the last two years of mission lifetime is shown in the right part of Figure 2, together with the mean daily change of altitude (green curve). The latter was about 50 m/days during the year 2009, but increased to a value of about 200 m/days during the first part of 2010, partly due to the fact that the satellite was turned by $180°$ in February 2010 (indicated by the dashed red vertical line). Before that date CHAMP flew with its boom in flight direction, which is a favorable condition regarding air drag but less optimal for attitude control. Since February 2010 CHAMP flew with the boom backward, making attitude control easier. After July 2010 the daily altitude decay increased rapidly to values of 500 m/day and more.

Parameterization of the CHAOS-4 model follows closely that of the previous versions in the CHAOS model series: The model consists of spherical harmonic expansion coefficients describing the magnetic field vector in an *Earth-Centered Earth-Fixed (ECEF)* coordinate system, and sets of Euler angles needed to rotate the vector readings from the magnetometer frame to the star imager frame. The magnetic field vector in the ECEF frame, $\mathbf{B} = -\nabla V$, is derived from a magnetic scalar potential $V = V^{\text{int}} + V^{\text{ext}}$ consisting of a part, V^{int}, describing internal (core and crustal) sources, and a part, V^{ext}, describing external (mainly magnetospheric) sources (including their Earth-induced counterparts). Both parts are expanded in terms of spherical harmonics.

For the internal part this yields

$$V^{\text{int}} = a \sum_{n=1}^{N_{\text{int}}} \sum_{m=0}^{n} (g_n^m \cos m\phi + h_n^m \sin m\phi) \left(\frac{a}{r}\right)^{n+1} P_n^m (\cos\theta)$$

$$(1)$$

where $a = 6371.2$ km is a reference radius, (r, θ, ϕ) are geographic coordinates, P_n^m are the associated Schmidt semi-normalized Legendre functions, $\{g_n^m, h_n^m\}$ are the Gauss coefficients describing internal sources, and N_{int} is the maximum degree and order of the internal expansion.

As mentioned before, the final CHAOS-4 model is found by merging two sub-models, called CHAOS-4l, resp.

CHAOS-4h. They differ in maximum spherical harmonic degree N_{int} of the static field, in the temporal parameterization of the low-degree (core field) terms, and in the data sets that have been used to derive these sum-models. Details are given below in sections 2.1 and 2.2.

Common for both sub-models is the parameterization of external fields, with an expansion of the remote magnetospheric sources (magnetotail and magnetopause) in *Geocentric Solar Magnetospheric (GSM)* coordinates (up to $n = 2$) and of near magnetospheric sources (magnetospheric ring current) in the *Solar Magnetic (SM)* coordinate system (also up to $n = 2$):

$$\begin{aligned}
V^{\text{ext}} &= a \sum_{n=1}^{2} \sum_{m=0}^{n} (q_n^m \cos mT_d + s_n^m \sin mT_d) \left(\frac{r}{a}\right)^n P_n^m (\cos\theta_d) \\
&+ a \sum_{m=0}^{1} (\hat{q}_1^m \cos T_d + \hat{s}_1^m \sin T_d) \cdot \left\{ E_{\text{st}}(t) \left(\frac{r}{a}\right) + I_{\text{st}}(t) \left(\frac{a}{r}\right)^2 \right\} \\
&+ a \sum_{n=1}^{2} q_n^{0,\text{GSM}} R_n^0(r, \theta, \phi)
\end{aligned}$$

where θ_d and T_d are dipole co-latitude and dipole local time, respectively.

The time dependence of degree-1 magnetospheric terms in SM coordinates is parametrized by the E_{st} and I_{st} indices [*Maus and Weidelt*, 2004; *Olsen et al.*, 2005]. In addition, we solve for large-scale time-varying degree-1 external coefficients in bins of 12 hours length (for $m = 0$), or 5 days length (for $m = 1$), similar to previous CHAOS model versions.

As part of the field modelling we co-estimate the Euler angles of the rotation between the coordinate systems of the vector magnetometer and of the star sensor providing attitude information. This part of model parametrization is also similar to that used for CHAOS-2 and CHAOS-3.

In following we will describe in more detail the different data and model parametrization used for the two sub-models.

2.1. CHAOS-4l

CHAOS-4l is determined using the whole data set (Ørsted, CHAMP and SAC-C satellite data plus observatory monthly means) described above, with a sampling rate of the satellite data of 60 seconds.

The maximum spherical harmonic degree of the internal field, $N_{\text{int}} = 60$, is similar as for CHAOS-2 and -3. Internal Gauss coefficients $\{g_n^m(t), h_n^m(t)\}$ up to $n = 20$

are time dependent; this dependence is described by order 6 B-splines [*Schumaker*, 1981; *De Boor*, 2001] with a 6-month knot separation and five-fold knots at the endpoints, $t = 1997.0$ and $t = 2011.0$. This yields 29 interior knots (at 1997.5, 1998.0, . . . , 2010.5) and 6 exterior knots at each endpoint, 1997.0 and 2011.0, resulting in 33 basic B-spline functions, $M_l(t)$. Internal Gauss coefficients for degrees $n = 21 - 60$ are static. Time-dependent terms (for degrees $n = 1 - 20$) and static terms (for $n = 21 - 60$) together result in a total of 15,760 internal Gauss coefficients. Together with the 7,024 model parameters describing the external field and the 828 parameters for the Euler angles this yields a total number of model parameters of 15,760 + 7,024 + 828 = 23,612.

These model parameters are estimated by means of a regularized *Iteratively Reweighted Least-Squares* approach using Huber weights, minimizing the cost function

$$\mathbf{e}^T \underline{\underline{C}}^{-1} \mathbf{e} + \lambda_3 \mathbf{m}^T \underline{\underline{\Lambda}}_3 \mathbf{m} + \lambda_2 \mathbf{m}^T \underline{\underline{\Lambda}}_2 \mathbf{m} \qquad (3)$$

where $\mathbf{m}$ is the model vector, the residuals vector $\mathbf{e} = \mathbf{d}_{\mathrm{obs}} - \mathbf{d}_{\mathrm{mod}}$ is the difference between observation $\mathbf{d}_{\mathrm{obs}}$ and model prediction $\mathbf{d}_{\mathrm{mod}}$, and $\underline{C}$ is the data covariance matrix. $\underline{\underline{\Lambda}}_3$ and $\underline{\underline{\Lambda}}_2$ are block diagonal regularization matrices which constrains the third, respectively second, order time derivatives of the core field. Contrary to previous versions in the CHAOS model series, for which the field intensity, $|\mathbf{B}|$, is regularized, we have chosen to constrain the radial field component, B_r, for CHAOS-4. $\underline{\underline{\Lambda}}_3$ minimizes the mean squared magnitude of $\left| \frac{\partial^3 B_r}{\partial t^3} \right|$, integrated over the core surface Ω_c (radius $c = 3485$ km) and averaged over time:

$$\left\langle \left| \frac{\partial^3 B_r}{\partial t^3} \right|^2 \right\rangle = \frac{1}{\Delta t} \int_{t=1997}^{2011} \int \left| \frac{\partial^3 B_r}{\partial t^3} \right|^2 d\Omega_c \, dt = \mathbf{m}^T \underline{\underline{\Lambda}}_3 \mathbf{m} \quad (4)$$

with $\Delta t = 2011.0 - 1997.0 = 13$ yrs.

Regularization of the third time derivative alone leads to oscillating field behavior. To avoid this we also minimize $|\ddot{B}_r|^2$ at the core surface at the model endpoints $t = 1997.0$ and 2011.0. This is implemented via the regularization matrix $\underline{\underline{\Lambda}}_2$. Note that $\underline{\underline{\Lambda}}_2$ only acts on 12 (the first and last six) of the 33 spline basis functions.

The two parameters λ_3 and λ_2 control the strength of the regularizations. We considered several values for these parameters and finally selected $\lambda_3 = 1 \ (\mathrm{nT/yr}^3)^{-2}$ and $\lambda_2 = 10 \ (\mathrm{nT/yr}^2)^{-2}$.

2.2. CHAOS-4h

CHAOS-4h is the high-degree part of the CHAOS-4 model. It is derived solely from CHAMP data obtained between January 2009 and September 2010. Data sampling interval is 30 seconds. Maximum spherical harmonic degree of the internal model part is $N_{\mathrm{int}} = 100$. A linear time dependence is used to describe the temporal variation of core field coefficients up to degree $n = 16$; coefficients between $n = 17$ to 100 are assumed to be static. No temporal regularization is applied, but for spherical harmonic degrees above $n = 85$ we minimize the mean value of $|B_r|$ averaged over the Earth's surface.

Similar to eq. 2 we minimize the cost function

$$\mathbf{e}^T \underline{\underline{C}}^{-1} \mathbf{e} + \lambda_0 \mathbf{m}^T \underline{\underline{\Lambda}}_0 \mathbf{m} \qquad (5)$$

using *Iteratively Reweighted Least-Squares* with Huber weights, where $\underline{\underline{\Lambda}}_0$ constrains the mean squared magnitude of $|B_r|$ for $n > 85$, integrated over the Earth surface Ω_a (radius $r = a$):

$$\langle |B_r|^2 \rangle = \int |B_r|^2 \, d\Omega_a \, dt = \mathbf{m}^T \underline{\underline{\Lambda}}_0 \mathbf{m}. \qquad (6)$$

$\underline{\underline{\Lambda}}_0$ is a diagonal matrix with elements $(n+1)^2/(2n+1)$ for $n > 95$, zero elements for $n < 85$, and a smooth transition between $n = 85$ and $n = 95$. We have chosen a damping parameter of $\lambda_0 = 3.3 \ \mathrm{nT}^{-2}$

When estimating high-degree magnetic field models using near-polar orbiting satellites special attention has to be paid to the polar gaps, which are the regions around the geographic poles of half-angle $|90° - i|$ where i is the inclination of the orbit. For CHAMP this values is $i = 87.3°$, which results in a polar gap of half-angle $2.7°$. Such a gap is especially a problem for the proper determination of zonal coefficients above $n = 60$. To avoid ringing at the poles we therefore add to the CHAMP magnetic field data synthetic scalar field values, synthesized within the polar gap from model CHAOS-4l (which only goes up to $n = 60$).

2.3. Merging the two sub-models CHAOS-4l and CHAOS-4h

The final CHAOS-4 model is obtained by combining the spherical harmonic coefficients of the two sub-models CHAOS-4 and CHAOS-4h. Spherical harmonic coefficients up to $n = 24$ (which includes the time-changing core field) and the external field are taken from CHAOS-4l, while the crustal field coefficients for degrees $n = 25$ to 100 are taken from CHAOS-4h. $n = 25$ was chosen as the transition degree since it was found that degree correlation ρ_n between the two models reaches a maximum of $\rho_n = 0.996$ at that degree while the relative difference (degree variance of model difference divided by degree variance of CHAOS-4 is less than 1%) is minimal.

3. Results and discussion

The total number of data points, residual means and root mean squared (rms) values of the two model versions are listed in Table 1. Means and rms are the weighted values calculated from the model residuals $e = d_{\mathrm{obs}} - d_{\mathrm{mod}}$ using the Huber weights w obtained in the last iteration. The obtained rms-misfit values (about 2.5 nT for the magnetic field intensity at non-polar latitudes and 4 to 6 nT at polar latitudes) are comparable to those of the previous versions of the CHAOS model series. Note that solving for the crustal field up to degree $n = 100$ (CHAOS-4h) reduces the CHAMP rms misfit only marginally compared to solving only up to $n = 60$ (CHAOS-4l), indicating the weakness of the high-degree crustal field signal at satellite altitude.

Despite of that a remarkable improvement in the determination of the lithospheric field is possible by taking advantage of the low-altitude CHAMP data. The right part of Figure 3 shows the spatial power spectrum of CHAOS-4 (black dots) and of various versions of the MF model series determined by Stefan Maus and co-workers. Up to spherical harmonic degree $n = 80$ the power of CHAOS-4 is very similar to that of MF7 [*Maus*, 2010], which is the most recent version in the MF model series. The power of previous versions in the MF series is though smaller than that of MF7 and CHAOS-4. Noteworthy is how the spectral power of the MF models increases with increasing version number: for degrees $n = 16 - 60$ the power of MF5 is 15% below that of CHAOS-4 while it is similar to that of CHAOS-4 within 1% for the later versions MF6 and MF7. For higher degrees ($n = 61 - 80$) the power of MF6 is as much as 30% below that of CHAOS-4. The underestimation of the lithospheric signal by MF6 has been corrected for with MF7, the power of which is very close to that of CHAOS-4. This

Table 1. Number N of data points, mean, and rms misfit (in nT for the satellite data, and in nT/yr for the observatory data) for CHAOS-4l and CHAOS-4h.

		component	CHAOS-4l			CHAOS-4h		
			N	mean	rms	N	mean	rms
satellite	Ørsted	F_{polar}	114,312	0.92	4.27			
		$F_{\text{nonpolar}} + B_B$	412,765	0.42	2.26			
		$B_\perp$	144,515	-0.04	7.72			
		B_3	144,515	-0.01	3.62			
	CHAMP	F_{polar}	149,130	-0.86	6.63	158,856	-0.89	6.57
		$F_{\text{nonpolar}} + B_B$	268,559	-0.59	2.47	286,535	-0.61	2.46
		$B_\perp$	254,289	0.01	3.50	272,123	0.01	3.51
		B_3	254,289	0.02	3.54	272,123	0.02	3.56
	SAC-C	F_{polar}	35,329	0.02	4.21			
		F_{nonpolar}	143,540	0.13	2.62			
observatory		dX/dt	15,756	-0.26	7.26			
		dY/dt	15,756	-0.12	4.91			
		dZ/dt	15,756	0.10	6.88			

change in power illustrates the effect of high-pass filtering that is used for deriving the MF models; earlier model versions have been derived using heavier filtering compared to more recent versions, which resulted in a lithospheric signal of reduced amplitude. Filtering is relaxed for the most recent versions of the MF series which clearly results in increased lithospheric signal. For MF7 filtering is only applied for degrees above $n = 77$; up to that degree CHAOS-4 and MF7 are very similar. The above mentioned finding regarding the effect of along-track filtering indicates that MF7 probably underestimates the crustal field signal for degrees above $n = 77$. The upcoming *Swarm* constellation mission consisting of three identical satellites, two of which are flying side-by-side at low altitude, will give an excellent opportunity to investigate this further. Experiments based on synthetic data have shown that the crustal field up to degree $n = 150$ can be robustly determined without along-track filtering [*Sabaka and Olsen*, 2006; *Olsen et al.*, 2007; *Tøffner-Clausen et al.*, 2010].

In addition to the spectra of the various crustal field signal, the left part of figure 3 shows also the spectra of the differences between CHAOS-4 and various other field models, which is smallest when comparing CHAOS-4 with MF7. These differences give an indication of the present uncertainty in crustal field modeling. The fact that the crustal field power is well above the power of the difference between CHAOS-4 and MF7 – two models which have been derived using fairly different approaches – confirms that crustal field structures at least up to degree $n = 80$, corresponding to a horizontal wavelength of 500 km, are currently robustly determined.

The right part of Figure 3 shows degree correlation ρ_n (see eq. (4.23) of *Langel and Hinze* [1998] for a definition) between CHAOS-4 and various other field models. Highest correlation is obtained with MF7, where degree correlation is above 0.97 for $n \leq 60$ and above 0.85 up to $n \leq 80$.

The left part of Figure 4 shows the sensitivity matrix $S(n, m)$, which is the relative difference of each coefficient of CHAOS-4 and MF7 in a degree versus order matrix; the right part shows that of the difference CHAOS-4 and MF6. Also this figure confirms the better agreement between CHAOS-4 and MF7 compared to MF6. There exist, however, certain spherical harmonic orders for which the difference between CHAOS-4 and MF7 is especially large, for instance around $m = 60$.
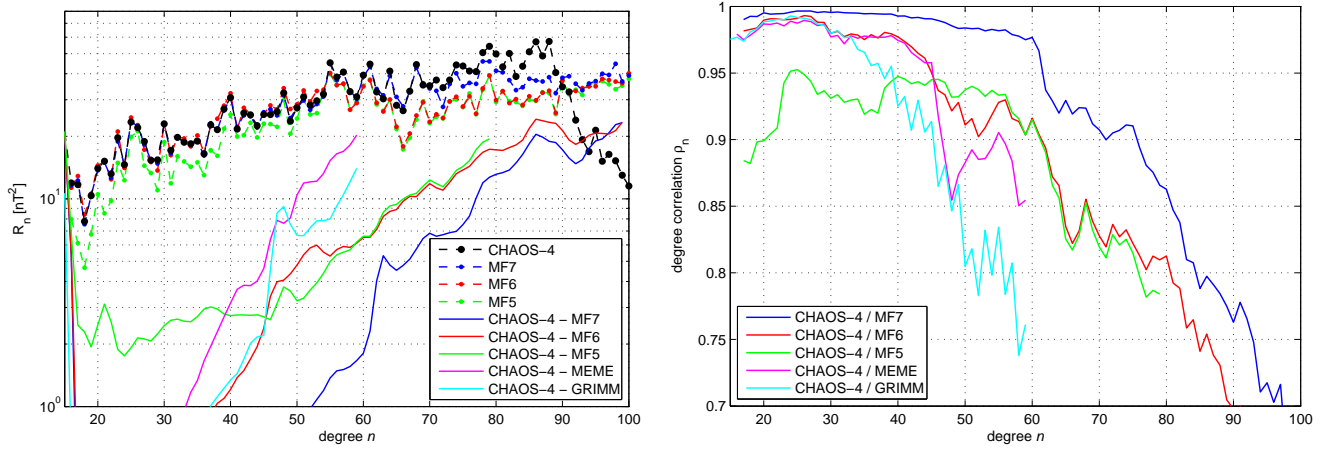
Figure 3. Left: Power spectra of the static field (dots) and of the field differences (solid lines). Right: Degree correlation for various models.
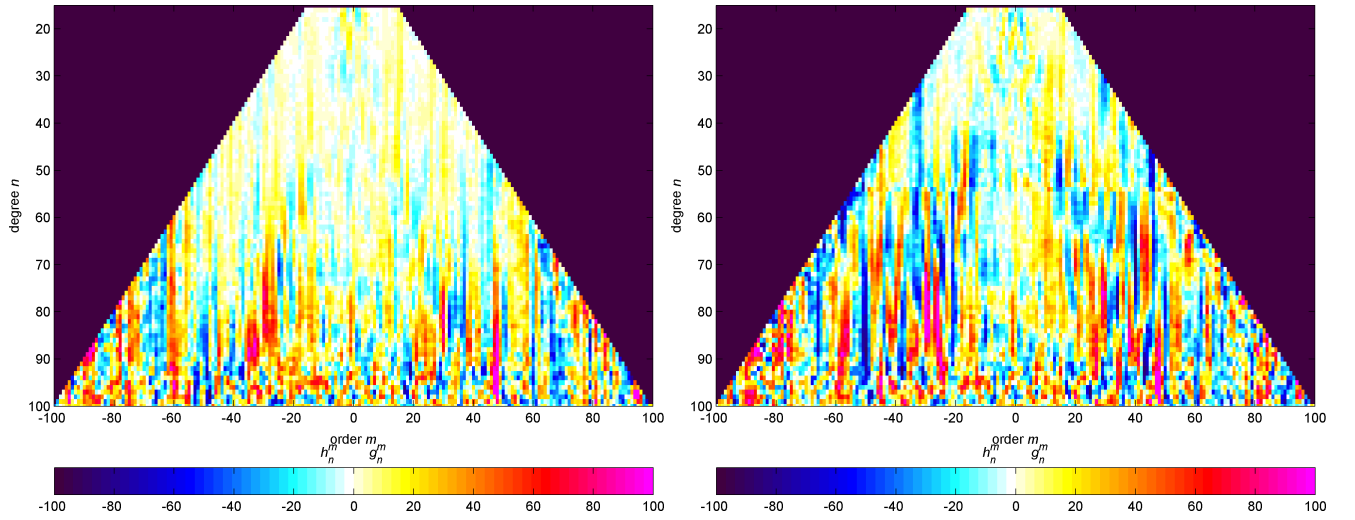

Figure 4. Sensitivity matrix (normalized coefficient differences in %) between CHAOS-4 and MF7 (left), resp. MF6 (right).
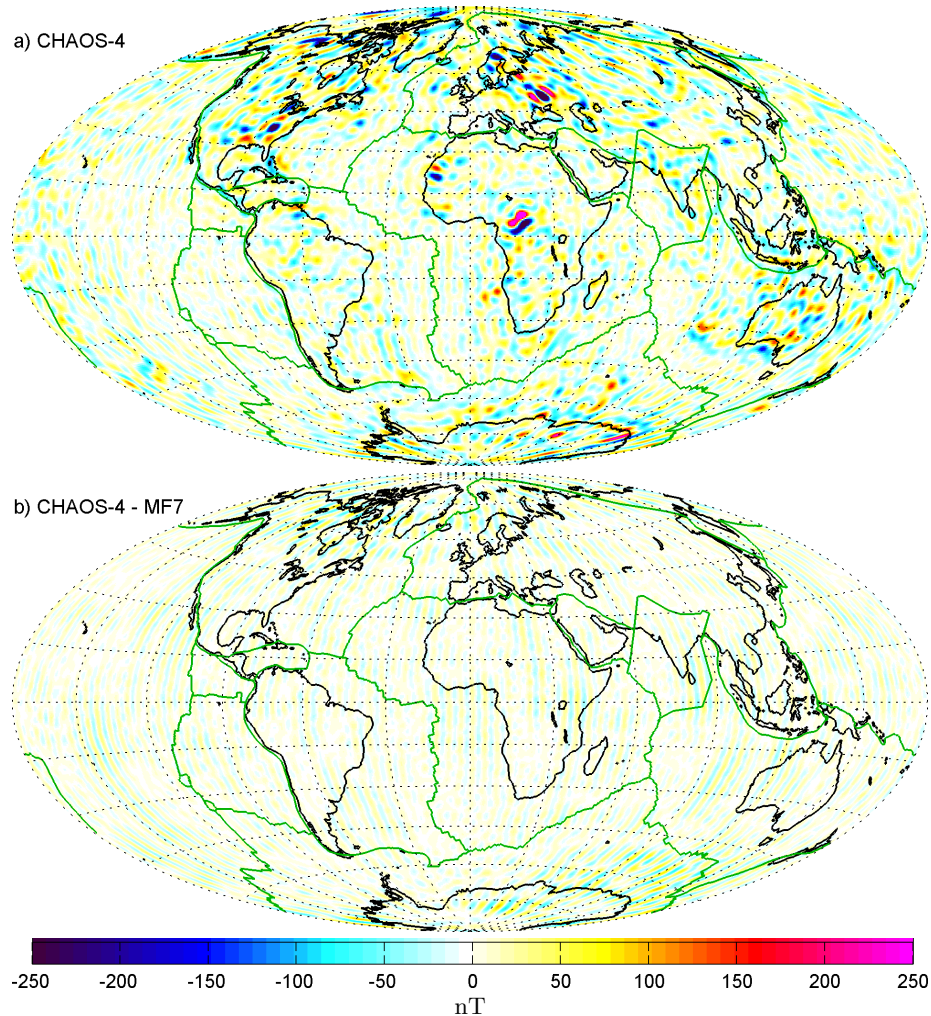
Figure 5. Top: Map of the radial magnetic field (in nT) at ground, calculated from coefficients of degrees $n = 16 - 100$. Bottom: radial field differences between CHAOS-4 and MF7.

4. Conclusions

Coefficients and data sets for the CHAOS-4 model versions are available at www.space.dtu.dk/files/magnetic-models/CHAOS-4/.

References

De Boor, C. (2001), A practical guide to splines, *Applied Mathematical Sciences*, *27*.

Holme, R. (2000), Modelling of attitude error in vector magnetic data: application to Ørsted data, *Earth, Planets and Space*, *52*, 1187–1197.

Holme, R., and J. Bloxham (1996), The treatment of attitude errors in satellite geomagnetic data, *Phys. Earth Planet. Int.*, *98*, 221–233.

Langel, R. A., and W. J. Hinze (1998), *The magnetic field of the Earth's lithosphere: The satellite perspective*, Cambridge University Press, Cambridge.

Lesur, V., I. Wardinski, M. Rother, and M. Mandea (2008), GRIMM: the GFZ Reference Internal Magnetic Model based on vector satellite and observatory data, *Geophys. J. Int.*, *173*, 382–294.

Lesur, V., I. Wardinski, S. Asari, B. Minchev, and M. Mandea (2010), Modelling the Earth's core magnetic field under flow constraints, *Earth, Planets and Space*, *62*, 503–516.

Maus, S. (2010), Magnetic field model MF7, www.geomag.us/models/MF7.html.

Maus, S., and P. Weidelt (2004), Separating the magnetospheric disturbance magnetic field into external and transient internal contributions using a 1D conductivity model of the Earth, *Geophys. Res. Lett.*, *31*, L12,614, doi:10.1029/2004GL020232.

Maus, S., F. Yin, H. Lühr, C. Manoj, M. Rother, J. Rauberg, I. Michaelis, C. Stolle, and R. Müller (2008), Resolution of direction of oceanic magnetic lineations by the sixth-generation lithospheric magnetic field model from CHAMP satellite magnetic measurements, *Geochem. Geophys. Geosyst.*, *9*(7), Q07,021, doi:10.1029/2008GC001949.

Olsen, N., and M. Mandea (2008), Rapidly changing flows in the Earth's core, *Nature Geoscience*, *1*(6), 390.

Olsen, N., T. J. Sabaka, and F. Lowes (2005), New parameterization of external and induced fields in geomagnetic field modeling, and a candidate model for IGRF 2005, *Earth, Planets and Space*, *57*, 1141–1149.

Olsen, N., H. Lühr, T. J. Sabaka, M. Mandea, M. Rother, L. Tøffner-Clausen, and S. Choi (2006), CHAOS – a model of Earth's magnetic field derived from CHAMP, Ørsted, and SAC-C magnetic satellite data, *Geophys. J. Int.*, *166*, 67–75, doi:10.1111/j.1365-246X.2006.02959.x.

Olsen, N., T. J. Sabaka, and L. Gaya-Pique (2007), Study of an improved comprehensive magnetic field inversion analysis

for *Swarm*, *DNSC Scientific Report 1/2007*, Danish National Space Center, Copenhagen.

Olsen, N., M. Mandea, T. J. Sabaka, and L. Tøffner-Clausen (2009), CHAOS-2 – A Geomagnetic Field Model Derived from one Decade of Continuous Satellite Data, *Geophys. J. Int.*, *179*(3), 1477–1487, doi:10.1111/j.1365-246X.2009.04386.x.

Olsen, N., M. Mandea, T. J. Sabaka, and L. Tøffner-Clausen (2010), The CHAOS-3 Geomagnetic Field Model and Candidates for the 11th Generation of IGRF, *Earth, Planets and Space*, *62*, 719–727.

Sabaka, T. J., and N. Olsen (2006), Enhancing comprehensive inversions using the *Swarm* constellation, *Earth, Planets and Space*, *58*, 371–395.

Sabaka, T. J., N. Olsen, and M. E. Purucker (2004), Extending comprehensive models of the Earth's magnetic field with Ørsted and CHAMP data, *Geophys. J. Int.*, *159*, 521–547, doi:10.1111/j.1365-246X.2004.02421.x.

Schumaker, L. L. (1981), *Spline functions: Basic theory*, John Wiley & Sons, New York.

Stolle, C., H. Lühr, M. Rother, and G. Balasis (2006), Magnetic signatures of equatorial spread *F*, as observed by the CHAMP satellite, *J. Geophys. Res.*, *111*, A02,304, doi: 10.1029/2005JA011,184.

Thébault, M. Purucker, K. A. Whaler, B. Langlais, and T. J. Sabaka (2010), The magnetic field of the Earth's lithosphere, *Space Sci. Rev.*, *155*, 95–127, doi:10.1007/s11214-010-9667-6.

Thomson, A., B. Hamilton, S. Macmillan, and S. Reay (2010), A novel weighting method for satellite magnetic data and a new global magnetic field model, *Geophys. J. Int.*, *181*, 250260, doi:10.1111/j.1365-246X.2010.04510.x.

Thomson, A. W. P., and V. Lesur (2007), An improved geomagnetic data selection algorithm for global geomagnetic field modelling, *Geophys. J. Int.*, *169*(3), 951–963.

Tøffner-Clausen, L., T. J. Sabaka, and N. Olsen (2010), End-To-End Mission Simulation Study (E2E+), in *Proceedings of the Second International Swarm Science Meeting*, ESA, Noordwijk/NL.

Nils Olsen, DTU Space, Juliane Maries Vej 30, 2100 Copenhagen, Denmark. (nio@space.dtu.dk)

Hermann Lühr, Helmholtz-Zentrum Potsdam, Deutsches GeoForschungsZentrum, 14473 Potsdam, Germany.

Terence J. Sabaka, Geodynamics Branch, NASA GSFC, Greenbelt/MD, USA.

Ingo Michaelis, Helmholtz-Zentrum Potsdam, Deutsches GeoForschungsZentrum, 14473 Potsdam, Germany.

Jan Rauberg, Helmholtz-Zentrum Potsdam, Deutsches GeoForschungsZentrum, 14473 Potsdam, Germany.

Lars Tøffner-Clausen, DTU Space, Juliane Maries Vej 30, 2100 Copenhagen, Denmark.

Chris C. Finlay, DTU Space, Juliane Maries Vej 30, 2100 Copenhagen, Denmark.